

Cramér–Rao Bound Optimization for Near-Field Sensing with Continuous-Aperture Arrays

Hao Jiang, *Graduate Student Member, IEEE*, Zhaolin Wang, *Member, IEEE*,
Yuanwei Liu, *Fellow, IEEE*, and Arumugam Nallanathan, *Fellow, IEEE*

Abstract—A Cramér–Rao bound (CRB) optimization framework for near-field sensing (NISE) with continuous-aperture arrays (CAPAs) is proposed. In contrast to conventional spatially discrete arrays (SPDAs), CAPAs emit electromagnetic (EM) probing signals through continuous source currents for target sensing, thereby exploiting the full spatial degrees of freedom (DoFs). The maximum likelihood estimation (MLE) method for estimating target locations in the near-field region is developed. To evaluate the NISE performance with CAPAs, the CRB for estimating target locations is derived based on continuous transmit and receive array responses of CAPAs. Subsequently, a CRB minimization problem is formulated to optimize the continuous source current of CAPAs. This results in a non-convex, integral-based functional optimization problem. To address this challenge, the optimal structure of the source current is derived and proven to be spanned by a series of basis functions determined by the system geometry. To solve the CRB minimization problem, a low-complexity subspace manifold gradient descent (SMGD) method is proposed, leveraging the derived optimal structure of the source current. Our simulation results validate the effectiveness of the proposed SMGD method and further demonstrate that i) the proposed SMGD method can effectively solve the CRB minimization problem with reduced computational complexity, and ii) CAPA achieves a tenfold improvement in sensing performance compared to its SPDA counterpart, due to full exploitation of spatial DoFs.

Index Terms—Cramér–Rao bound optimization, continuous-aperture array (CAPA), near-field sensing (NISE).

I. INTRODUCTION

RAPID evolution of communication technologies is steering the development of the next-generation telecommunication networks to support not only high-speed data transmission but also advanced sensing capabilities [1]. The unprecedented performance gains offered by multiple-input and multiple-output (MIMO) in communication inspire its application to sensing. Compared with conventional sensing setups, MIMO-based sensing offers a high spatial resolution while alleviating the reliance on formidable bandwidth requirement [2], [3]. Given these benefits, MIMO has become a pivotal technology for 6G sensing.

In contrast to the current 5G networks operating at the 3.5 GHz band, the upcoming 6G networks are expected to operate at high-frequency bands, such as mmWave bands and sub-terahertz bands [4]. These bands can provide extensive

spectrum availability for the communication functionality and enable high spatial resolution for the integrated sensing functionality [2]. However, two major issues will arise when the high carrier frequencies are utilized. On the one hand, due to a shrinking wavelength, more antennas will be placed in given areas, thus driving an evolution from massive MIMO (mMIMO) to gigantic MIMO (gMIMO), and eventually to continuous aperture arrays (CAPAs). Compared to conventional spatially discrete arrays (SPDAs) like MIMO, CAPAs can be regarded as an integration of an infinite number of antennas, thus forming a spatially continuous antenna aperture and boosting the sensing accuracy [5]. On the other hand, high carrier frequencies on these bands can inherently give rise to well-known near-field phenomena, resulting in spherical wave propagation instead of planar wave propagation in space [6]. In this case, the conventional planar wavefront assumption does not hold anymore. From a near-field sensing (NISE) perspective, the curvatures of the impinging spherical wavefronts allow for more comprehensive sensing, including both distance and angle.

A. Prior Works

1) *Near-Field Sensing with SPDAs*: NISE with spatially discrete arrays (SPDAs) has become a “hotspot” of research and has been extensively investigated [7]–[13]. Specifically, the authors of [7] demonstrated that, unlike the far-field angle-only sensing, NISE enables joint sensing of targets’ angle and distance by exploiting the curvature of impinging spherical wavefront in the near-field regions. Building on this unique polar-domain dependence, the authors of [8] proposed a low-complexity multiple signal classification (MUSIC) algorithm to localize multiple sensing targets, where a two-dimensional (2D) MUSIC spectrum is searched. In a separate study, the authors of [9] developed a sensing-performance optimization algorithm for near-field integrated sensing and communication (ISAC) systems. To quantify the sensing performance analytically, the Cramér–Rao bound (CRB) is widely adopted in NISE tasks as the lower bound for unbiased estimators. Specifically, the authors of [10] and [11] derived the conditional and unconditional CRBs for mono-static and bi-static NISE systems. The above studies are within the scope of low-mobility or static sensing scenarios, where the sensing target is assumed to remain stationary for a relatively long time. For the mobility NISE tasks, [12] and [3] showed that it is possible to simultaneously estimate both radial and transverse velocities of a moving target by leveraging the Doppler frequencies. On top

Hao Jiang, Zhaolin Wang, and Arumugam Nallanathan are with the School of Electronic Engineering and Computer Science, Queen Mary University of London, London E1 4NS, U.K. (e-mail: {hao.jiang; zhaolin.wang; a.nallanathan}@qmul.ac.uk).

Yuanwei Liu is with the Department of Electrical and Electronic Engineering, The University of Hong Kong, Hong Kong (e-mail: yuanwei@hku.hk).

of this observation, the authors of [12] proposed a predictive beamforming scheme for near-field mobility networks, while [13] analyzed the CRBs for the radial and transverse velocity sensing in such scenarios.

2) *Near-Field Sensing with CAPAs*: Unlike the extensive research efforts for NISE in SPDAs, research on CAPA-based NISE is still in its early stages and primarily focuses on active positioning scenarios, where the sensing target needs to transmit a dedicated signal to the receiver actively. Due to the electromagnetic (EM)-based channel modeling for CAPAs, the channel response (or received electric field) is a function of both distance and angle, allowing for joint angle and distance estimation in the near-field regions. For instance, the authors of [2] analyzed a CAPA-based positioning system, where the target (a Hertzian dipole) transmits probing signals actively to a holographic surface with a continuous aperture. In light of the EM theory, CRB was derived for this setup, providing the lower bound for maximum likelihood estimation (MLE) of the target's position. Considering both scalar and vector electric field scenarios, the authors of [14] extended the analysis by deriving CRBs for a similar active positioning system in the near-field region. This work demonstrated that centimeter-level sensing accuracy can be achieved in the near field of a receiving antenna array with a practical aperture size operating in mmWave or sub-THz bands. Additionally, the authors of [15] investigated the expected CRB (ECRB) and Ziv-Zakai bound (ZZB) for joint position and attitude estimation within the near-field region, considering a similar active sensing setup.

B. Motivations and Contributions

Despite the fruitful research endeavors in prior works, the majority of the existing literature on CAPA-based NISE falls in the category of active sensing, where the sensing target needs to transmit dedicated probing signals to the receiver actively. With the growing trend of integrating sensing and communication functionalities into a shared antenna array in 6G [16], passive sensing is also worth investigating, which alternatively utilizes the reflected probing signal to position the targets themselves. Hence, passive sensing can exempt the need for dedicated probing signals from the target. To enable CAPA-based passive NISE systems, three key challenges must be addressed: **First, a positioning algorithm is required for CAPA-based passive NISE scenarios.** Compared to active sensing, passive sensing lacks dedicated probing signals from the target, making accurate positioning more challenging. **Second, a sensing performance bound specifically for CAPA-based NISE scenarios needs to be derived, based on which the sensing performance can be quantified.** Moreover, this sensing performance bound needs to be derived based on a continuous source function and must be tractable to allow for further optimization. **Third, a sensing-performance-bound optimization algorithm needs to be devised to enhance the sensing accuracy.** It is noteworthy that, in contrast to discrete-variable-based optimizations in conventional SPDAs, CAPA-based passive sensing requires optimizing a continuous source current.

Currently, the most widely adopted method is the wavenumber-domain method [17], which discretizes the continuous source current function by sampling a finite number of points in the wavenumber domain. By doing so, instead of directly dealing with a continuous function, Fourier coefficients are optimized equivalently, whose number is proportional to the carrier frequency. Although this approach is straightforward, its complexity is prohibitive due to the high volume of Fourier coefficients, particularly for planar arrays operating at high frequencies. Therefore, dealing with the three challenges with affordable complexity plays a fundamental role for CAPA-based passive NISE systems.

To bridge the knowledge gap, this paper aims to address the three key challenges by deriving a performance bound for multi-target NISE scenarios and proposing a manifold-based optimization method to enhance sensing accuracy. Our main contributions are summarized as follows:

- We model the round-trip channel for CAPA-based NISE based on EM theories, where the base station (BS) is equipped with two separate Tx and Rx CAPAs to position the multiple targets in a passive sensing fashion.
- We propose an MLE-based method to estimate the positions of multiple targets based on EM-based round-trip channel modeling. This method is developed under the maximum likelihood rule.
- We derive the CRB for the above setup, providing a mathematically tractable lower bound for sensing performance. Based on the derived CRB, a CRB minimization problem is formulated under a unit power constraint. By solving this problem, the sensing accuracy can be improved.
- We prove that the optimal solution resides in a sub-space spanned by the array responses of all the sensing targets. Subsequently, we propose a low-complexity subspace manifold gradient descent (SMGD) to solve the CRB minimization problem.
- We present numerical results to verify the performance of the proposed SMGD method and provide insights into the CRB in CAPA-based systems. The simulation results demonstrate that: i) The proposed SMGD algorithm can solve the CRB minimization problem effectively at a reduced cost of computational complexity. ii) The achieved CRB of CAPAs outperforms that of its SPDA counterpart, confirming CAPA's advanced sensing capabilities.

C. Organization and Notations

The organizations of this paper are showcased as follows. Section II presents the system model and the passive multi-target sensing signal model. The CRB and MLE spectra derivations are detailed in Section III. Based on the derivations in the former section, the CRB minimization problem is formulated and solved by the proposed SMGD algorithm in Section IV. Numerical results are elaborated in Section V to demonstrate the performance of the proposed algorithm. Finally, the conclusion is drawn in Section VI.

Notations: Scalars are denoted using regular typeface, while vectors and matrices are denoted by bold-face letters. $\Re\{\cdot\}$

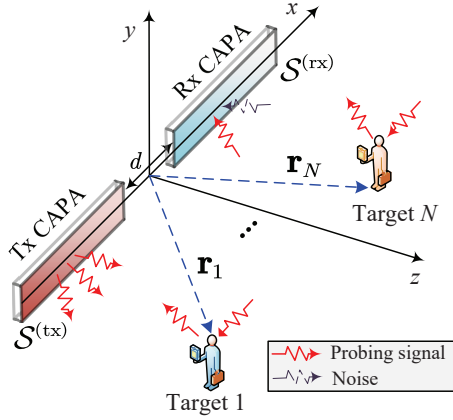


Fig. 1: An illustration of the CAPA-based NISE system setup.

and $\Re\{\cdot\}$ and $\Im\{\cdot\}$ are the operations to extract the real and imaginary parts of (\cdot) . $\text{Tr}\{\cdot\}$, $(\cdot)^T$, $(\cdot)^*$, $[(\cdot)]^{-1}$, and $\text{Rank}\{\cdot\}$ represent the trace, transpose, conjugate, matrix inverse, and calculating-rank operations, respectively. \mathbf{B}^{Tr} and \otimes denote the blockwise trace operation for a block matrix \mathbf{B} and the Kronecker product, respectively. $\langle \cdot, \cdot \rangle$ denotes the inner product between two continuous functions. $\mathbb{R}^{M \times N}$ and $\mathbb{C}^{M \times N}$ denote the $M \times N$ real and imaginary matrix spaces, respectively. $[(\cdot)]_{m,n}$ means to take the (m, n) -th entry of matrix/vector (\cdot) . $j = \sqrt{-1}$ is the imaginary unit.

II. SYSTEM MODEL

The system model of this work is presented in Fig. 1, where the BS is equipped with a Tx planar CAPA (P-CAPA) for transmission and an Rx P-CAPA for reception. There are N sensing targets being positioned by the BS. Without loss of generality, we assume that the Rx and Tx P-CAPAs are placed on the XOY plane, separated with a distance of d . The origin of the coordinate system is set at the center point between Rx and Tx P-CAPAs. It is noted that, due to the adoption of P-CAPAs, channel responses across the z -axis are negligible [18]. Further, we assume the targets are located within the radiating near-field region of the BS, which is defined by $r \leq \frac{2D^2}{\lambda}$ with D and λ denoting the aperture size and wavelength, respectively.

A. Green's Function-Based Channel Modeling

For the BS, the sizes of the Tx and Rx P-CAPAs are denoted by $H^{(\text{tx})} \times W^{(\text{tx})}$ and $H^{(\text{rx})} \times W^{(\text{rx})}$ respectively, where $H^{(\cdot)}$ and $W^{(\cdot)}$ denote the height and the width of the Rx and Tx P-CAPAs, respectively. The coordinate regions of the Tx and Rx P-CAPAs are specified by

$$\mathcal{S}^{(\text{tx})} = \left\{ \mathbf{p} \triangleq [p^{(x)}, p^{(y)}, p^{(z)}]^T : W_{\min}^{(\text{tx})} \leq p^{(x)} \leq W_{\max}^{(\text{tx})}, \right. \\ \left. H_{\min}^{(\text{tx})} \leq p^{(y)} \leq H_{\max}^{(\text{tx})}, p^{(z)} = 0 \right\}, \quad (1)$$

$$\mathcal{S}^{(\text{rx})} = \left\{ \mathbf{q} \triangleq [q^{(x)}, q^{(y)}, q^{(z)}]^T : W_{\min}^{(\text{rx})} \leq q^{(x)} \leq W_{\max}^{(\text{rx})}, \right. \\ \left. H_{\min}^{(\text{rx})} \leq q^{(y)} \leq H_{\max}^{(\text{rx})}, q^{(z)} = 0 \right\}, \quad (2)$$

where the boundaries are calculated by $W_{\min}^{(\text{tx})} = -W^{(\text{tx})} - d/2$, $W_{\max}^{(\text{tx})} = -d/2$, $W_{\min}^{(\text{rx})} = d/2$, $W_{\max}^{(\text{rx})} = W^{(\text{rx})} +$

$d/2$, $H_{\min}^{(\text{tx})} = -0.5H^{(\text{tx})}$, $H_{\max}^{(\text{tx})} = +0.5H^{(\text{tx})}$, $H_{\min}^{(\text{rx})} = -0.5H^{(\text{rx})}$, and $H_{\max}^{(\text{rx})} = +0.5H^{(\text{rx})}$, respectively. The position of the n -th ST is specified by $\mathbf{r}_n \triangleq [r_n^{(x)}, r_n^{(y)}, r_n^{(z)}]^T \in \mathbb{R}^{3 \times 1}$, where $n \in \mathcal{N}$ and $\mathcal{N} \triangleq \{1, 2, \dots, N\}$.

Due to the adoption of P-CAPAs, we adopt Green's function-based channel model [6], [19]–[21]. In particular, letting $\mathbf{p} \in \mathcal{S}^{(\text{tx})}$ and $\mathbf{q} \in \mathcal{S}^{(\text{rx})}$ be two arbitrary points on the Tx and the Rx P-CAPAs respectively, an electric field $\mathbf{E}(\mathbf{q}, w) \in \mathbb{C}^{3 \times 1}$ at the receiver will be excited by a current density $\mathbf{J}(\mathbf{p}, w) \in \mathbb{C}^{3 \times 1}$, where w denotes the angular frequency. Considering a narrow-band single-carrier system, the dependence on w in $\mathbf{E}(\mathbf{q}, w)$ and $\mathbf{J}(\mathbf{p}, w)$ can be discarded, thereby giving rise to a time-invariant expression $\mathbf{E}(\mathbf{q})$ and $\mathbf{J}(\mathbf{p})$. It is worth noting that $\mathbf{E}(\mathbf{q})$ and $\mathbf{J}(\mathbf{p})$ are tri-polarized vectors, meaning that they have components in three orthogonal directions. However, due to the practical challenge of implementing tri-polarized transmitters and receivers, we adopt a uni-polarized configuration aligned with [22] and [18]. In this configuration, only one polarization component of $\mathbf{E}(\mathbf{q})$ is utilized for transmission, while only one polarization component of $\mathbf{J}(\mathbf{p})$ is received at the receiver. Consequently, $\mathbf{E}(\mathbf{q})$ and $\mathbf{J}(\mathbf{p})$ are now scalars, and therefore can be simplified to $E(\mathbf{q}) = \hat{\mathbf{u}}^T \mathbf{E}(\mathbf{q})$ and $J(\mathbf{p}) = \hat{\mathbf{u}}^T \mathbf{J}(\mathbf{p})$ respectively, where $\hat{\mathbf{u}} \in \mathbb{R}^{3 \times 1}$ denotes a unit directional vector satisfying $\|\hat{\mathbf{u}}\|_2^2 = 1$.

Moreover, free-space dyadic Green's function denoted by $g(\cdot)$ is utilized to describe a mapping from a source current $J(\mathbf{p})$ to an induced radiating field $E(\mathbf{q})$. Specifically, for an vector \mathbf{v} , the dyadic Green's function can be expressed as

$$g(\mathbf{v}) = \frac{j\eta_0 e^{-jk_0 \|\mathbf{v}\|_2}}{2\lambda^2 \|\mathbf{v}\|_2} \left(1 + \frac{j}{k_0 \|\mathbf{v}\|_2} - \frac{1}{k_0^2 \|\mathbf{v}\|_2^2} \right), \quad (3)$$

where $\eta_0 = 120\pi$ denotes the intrinsic impedance of free space, and $k_0 \triangleq \frac{2\pi}{\lambda}$ denotes the wavenumber. The first term in the braces of (3) represents the effects of the radiating near-field and far-field regions, while the second and third terms jointly demonstrate the impact of the reactive near-field region. Moreover, it is essential to underscore that the reactive near-field region is omitted since it is confined within a few wavelengths [23]. Consequently, the expression of the transmit antenna response can be simplified by discarding high-order terms outlined by [23]–[25]. Thus, we can approximate the dyadic Green's function with the scalar Green's function, thus yielding:

$$g(\mathbf{v}) \approx \frac{j\eta_0 e^{-jk_0 \|\mathbf{v}\|_2}}{2\lambda^2 \|\mathbf{v}\|_2}. \quad (4)$$

In addition, the electric field at the receiver $E(\mathbf{q})$ induced by a source current at the transmitter $J(\mathbf{p})$ can be bridged by the Green's function $g(\mathbf{v})$ as outlined by [2], [14], [15].

B. Sensing Signal Modeling

In our system model, the round-trip channels need to be considered, consisting of both the probing and the echo spatial propagation model and the reflecting model between them. As illustrated in Fig. 2, for the n -th ST, we define the transmit vector as $\mathbf{k}_n \triangleq \mathbf{r}_n - \mathbf{p}$ and the receive vector $\boldsymbol{\kappa}_n \triangleq \mathbf{q} - \mathbf{r}_n$,

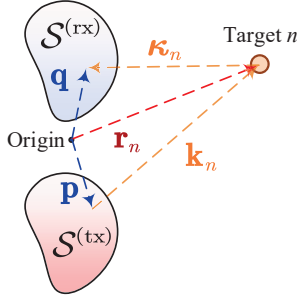


Fig. 2: An explanation of geometry for the n -th ST.

given that the coordinates $\mathbf{p} \in \mathcal{S}^{(\text{tx})}$ and $\mathbf{q} \in \mathcal{S}^{(\text{rx})}$ are of our interest. Thus, the probing channel response modeled by Green's function can be expressed as

$$g_t(\mathbf{k}) = \frac{j\eta_0 e^{-jk_0 \|\mathbf{k}\|_2}}{2\lambda^2 \|\mathbf{k}\|_2}. \quad (5)$$

In addition, considering the reciprocity theorem for antennas outlined by [25], the receive antenna response can be calculated by

$$g_r(\boldsymbol{\kappa}) = \frac{-j\eta_0 e^{jk_0 \|\boldsymbol{\kappa}\|_2}}{2\lambda^2 \|\boldsymbol{\kappa}\|_2}. \quad (6)$$

Now, the spatial propagation model of EM waves has been established. In the sequel, we will present the reflection model of EM waves. According to [25], for any transmit and receive directions $\hat{\mathbf{k}} \triangleq \frac{\mathbf{k}}{\|\mathbf{k}\|}$ and $\hat{\boldsymbol{\kappa}} \triangleq \frac{\boldsymbol{\kappa}}{\|\boldsymbol{\kappa}\|}$, the coupling response (or scattering response) can be expressed as

$$c(\hat{\boldsymbol{\kappa}}, \hat{\mathbf{k}}) = \frac{1}{\sqrt{N}} \sum_{n=1}^N \alpha_n \delta(\hat{\mathbf{k}} - \hat{\mathbf{k}}_n) \delta(\hat{\boldsymbol{\kappa}} - \hat{\boldsymbol{\kappa}}_n), \quad (7)$$

where $\alpha_n \in \mathbb{C}$ denotes the reflection coefficient of the n -th ST [16], and $\delta(\cdot)$ is the Dirac function. Therefore, jointly considering the reciprocity of the wireless channel, the round-trip channel can be specified by

$$\begin{aligned} h(\mathbf{q}, \mathbf{p}) &= \int_{\mathcal{A}} \int_{\mathcal{A}} g_r(\boldsymbol{\kappa}) c(\hat{\boldsymbol{\kappa}}, \hat{\mathbf{k}}) g_t(\mathbf{k}) d\hat{\boldsymbol{\kappa}} d\hat{\mathbf{k}} \\ &\stackrel{(a)}{=} c_0 \sum_{n=1}^N a_r(\boldsymbol{\kappa}_n) \alpha_n a_t(\mathbf{k}_n), \end{aligned} \quad (8)$$

where $c_0 \triangleq \frac{\eta_0^2}{4\lambda^4 \sqrt{N}}$, \mathcal{A} denotes the whole space, (a) is obtained using the property of Dirac function, and the transmit and receive responses of the n -th ST can be expressed as

$$a_t(\mathbf{k}_n) \triangleq \frac{1}{\|\mathbf{k}_n\|_2} e^{-jk_0 \|\mathbf{k}_n\|_2}, \quad (9)$$

$$a_r(\boldsymbol{\kappa}_n) \triangleq \frac{1}{\|\boldsymbol{\kappa}_n\|_2} e^{jk_0 \|\boldsymbol{\kappa}_n\|_2}. \quad (10)$$

In the sequel, we will present the noise model. Particularly, we assume that the noise term $n(\mathbf{q}) \in \mathbb{C}$ with $\mathbf{q} \in \mathcal{S}^{(\text{rx})}$ follows to a spatially uncorrelated zero-mean complex Gaussian process as described in [2] and [26]. The correlation function of such a process is given by

$$\mathbb{E}\{n(\mathbf{q})n^*(\mathbf{q}')\} = \sigma_0^2 \delta(\mathbf{q} - \mathbf{q}'), \quad (11)$$

where σ_0^2 denotes the power angular density measured by V^2 , where V represents volts. Here, a spatially white noise model is adopted for simplicity. For those interested in spatially colored noise modeling, further details can be found in [19]. It is worth noting that term $\delta(\mathbf{q} - \mathbf{q}')$ in (11) reveals that the noise is uncorrelated across different points \mathbf{q} and \mathbf{q}' on Rx P-CAPA.

On top of the above, due to the presence of noise, the received echo signal $y(\mathbf{q})$ at Rx P-CAPA can be expressed as

$$y(\mathbf{q}) = E(\mathbf{q}) + n(\mathbf{q}), \quad (12)$$

where the excited electric filed $E(\mathbf{q})$ is defined by

$$E(\mathbf{q}) \triangleq \int_{\mathcal{S}^{(\text{tx})}} h(\mathbf{q}, \mathbf{p}) J(\mathbf{p}) d\mathbf{p}. \quad (13)$$

In the considered CAPA-based passive NISE scenario, the Tx P-CAPA transmits probing signals with a designed source current function $J(\mathbf{p})$ over region $\mathcal{S}^{(\text{tx})}$. After the probing signal is reflected by the STs, the Rx P-CAPA receives the echo signal $E(\mathbf{q})$ received over region $\mathcal{S}^{(\text{rx})}$. Therefore, we aim to extract the targets' positional information $\{\mathbf{r}_i\}_{i=1, \dots, N}$ from the received echo signal $E(\mathbf{q})$ over the entire Tx P-CAPA $\mathcal{S}^{(\text{rx})}$. Since $\{\mathbf{r}_i\}_{i=1, \dots, N}$ is of interest, we mainly focus on the positioning accuracy.

III. DERIVATIONS OF MLE AND CRB

In this section, we first present the derivation of the MLE method, which is a positioning method for multiple targets under the maximum likelihood rule. Then, to characterize the sensing performance, we derive CRB as the performance metric, which is widely used in literature [16], [27], [28].

A. MLE Derivations for CAPAs

Given that the positions and the reflection coefficients of the N STs need to be estimated, the unknown parameter vector $\boldsymbol{\xi}$ can be expressed as

$$\begin{aligned} \boldsymbol{\xi} &= [\mathbf{r}_1, \dots, \mathbf{r}_N, \Re\{\alpha_1\}, \Im\{\alpha_1\}, \dots, \Re\{\alpha_N\}, \Im\{\alpha_N\}]^T \\ &= [\mathbf{r}, \boldsymbol{\alpha}]^T \in \mathbb{R}^{5N \times 1}, \end{aligned} \quad (14)$$

where $\mathbf{r} \triangleq [\mathbf{r}_1, \dots, \mathbf{r}_N]^T$ contains the positions of the N STs and $\boldsymbol{\alpha} \triangleq [\Re\{\alpha_1\}, \Im\{\alpha_1\}, \dots, \Re\{\alpha_N\}, \Im\{\alpha_N\}]^T$ contains the real and imaginary parts of the reflection coefficients of the N STs. For target positioning, \mathbf{r} can be estimated using classic MLE based on received observation $y(\mathbf{q})$ for $\mathbf{q} \in \mathcal{S}^{(\text{rx})}$. It is noted that, compared to conventional SPDA-based sensing, the derivation of MLE in this work is based on a continuous source current function. Based on the received echo signals denoted by $y(\mathbf{q})$, the estimated version of the unknown position vector $\hat{\mathbf{r}}$ can be obtained by maximizing the likelihood. The discrete expression log-likelihood function can be found in [2]. Based on this, by treating receive dipoles on the Rx P-CAPA as infinitesimals, the summation expression of

the likelihood function can be regarded as an integral, which can be expressed as

$$\begin{aligned}\mathcal{L} &= \lim_{d\mathbf{q} \rightarrow 0} \sum_{\mathbf{q} \in \mathcal{S}(\text{rx})} \left| y(\mathbf{q}) - \sum_{n=1}^N \alpha_n \tilde{E}_n(\mathbf{q}) \right|^2 \\ &= \int_{\mathcal{S}(\text{rx})} \left| y(\mathbf{q}) - \sum_{n=1}^N \alpha_n \tilde{E}_n(\mathbf{q}) \right|^2 d\mathbf{q} \\ &= \int_{\mathcal{S}(\text{rx})} \left(|y(\mathbf{q})|^2 - 2\Re \left\{ y(\mathbf{q}) \sum_{n=1}^N \alpha_n^* \tilde{E}_n^*(\mathbf{q}) \right\} \right. \\ &\quad \left. + \left| \sum_{n=1}^N \alpha_n \tilde{E}_n(\mathbf{q}) \right|^2 \right) d\mathbf{q},\end{aligned}\quad (15)$$

where $y(\mathbf{q})$ denotes the received signal, while $\tilde{E}_n(\mathbf{q}) \triangleq c_0 a_r(\boldsymbol{\kappa}_n) a_t(\mathbf{k}_n)$, aiming at excluding the reflection coefficient, α_n . To find the optimal solution for estimating α_n for $n \in \mathcal{N}$, we calculate the partial derivative with respect to α_n^* and let this derivative equals zero, thus yielding

$$\begin{aligned}\frac{\partial \mathcal{L}}{\partial \alpha_n^*} &= \\ &\int_{\mathcal{S}(\text{rx})} \frac{\partial}{\partial \alpha_n^*} \left(|y(\mathbf{q})|^2 - 2\Re \left\{ y(\mathbf{q}) \sum_{n=1}^N \alpha_n^* \tilde{E}_n^*(\mathbf{q}) \right\} \right. \\ &\quad \left. + \left| \sum_{n=1}^N \alpha_n \tilde{E}_n(\mathbf{q}) \right|^2 \right) d\mathbf{q} \\ &= \int_{\mathcal{S}(\text{rx})} \left(\tilde{E}_n^*(\mathbf{q}) \left(\sum_{n=1}^N \alpha_n \tilde{E}_n(\mathbf{q}) \right) - \tilde{E}_n^*(\mathbf{q}) y(\mathbf{q}) \right) d\mathbf{q} = 0,\end{aligned}\quad (16)$$

Then, by defining $\mathbf{E} \triangleq [\tilde{E}_1(\mathbf{q}), \dots, \tilde{E}_N(\mathbf{q})]^T$ and $\boldsymbol{\alpha} \triangleq [\alpha_1, \dots, \alpha_N]^T$, we have

$$(16) = \int_{\mathcal{S}(\text{rx})} \left(\tilde{E}_n^*(\mathbf{q}) \mathbf{E}^T \boldsymbol{\alpha} - \tilde{E}_n^*(\mathbf{q}) y(\mathbf{q}) \right) d\mathbf{q} = 0. \quad (17)$$

Since $\boldsymbol{\alpha}$ is independent to the integration variable \mathbf{q} , (17) can be written as a linear equation:

$$\boldsymbol{\rho}_n^T \boldsymbol{\alpha} = m_n,$$

where

$$\begin{aligned}m_n &\triangleq \int_{\mathcal{S}(\text{rx})} \tilde{E}_n^*(\mathbf{q}) y(\mathbf{q}) d\mathbf{q}, \\ \boldsymbol{\rho}_n &\triangleq \left[\int_{\mathcal{S}(\text{rx})} \tilde{E}_n^*(\mathbf{q}) \tilde{E}_1(\mathbf{q}) d\mathbf{q}, \dots, \int_{\mathcal{S}(\text{rx})} \tilde{E}_n^*(\mathbf{q}) \tilde{E}_N(\mathbf{q}) d\mathbf{q} \right]^T.\end{aligned}$$

The above derivations can be performed for $\forall n \in \mathcal{N}$, thus yielding a system of linear equations:

$$\mathbf{P} \boldsymbol{\alpha} = \mathbf{m}, \quad (18)$$

where

$$\mathbf{P} \triangleq [\boldsymbol{\rho}_1^T, \dots, \boldsymbol{\rho}_N^T]^T, \quad (19)$$

$$\mathbf{m} \triangleq [m_1, \dots, m_N]^T. \quad (20)$$

Therefore, the solution to (18) can be expressed as

$$\boldsymbol{\alpha} = \mathbf{P}^{-1} \mathbf{m}. \quad (21)$$

It is noted that since the targets are sparsely distributed in practical scenarios, \mathbf{P} is full-rank and invertible as a result of linearly independent rows. Therefore, by substituting the reflection coefficients in (15) with the results in (21), the likelihood function can be written as

$$\begin{aligned}\mathcal{L} &= \\ &\int_{\mathcal{S}(\text{rx})} \left(|y(\mathbf{q})|^2 - 2\Re \{ y^*(\mathbf{q}) \mathbf{E}^H \mathbf{P}^{-1} \mathbf{m} \} + |\mathbf{E}^T \mathbf{P}^{-1} \mathbf{m}|^2 \right) d\mathbf{q} \\ &= \int_{\mathcal{S}(\text{rx})} |y(\mathbf{q})|^2 d\mathbf{q} - 2\Re \left\{ \left(\int_{\mathcal{S}(\text{rx})} y^*(\mathbf{q}) \mathbf{E}^H d\mathbf{q} \right) \mathbf{P}^{-1} \mathbf{m} \right\} \\ &\quad + \text{Tr} \left\{ \left(\int_{\mathcal{S}(\text{rx})} \mathbf{E}^* \mathbf{E}^H d\mathbf{q} \right) \mathbf{P}^{-1} \mathbf{m} \mathbf{m}^H (\mathbf{P}^{-1})^H \right\}\end{aligned}$$

Then, we define the following quantities:

$$\mathbf{I}_1 = \int_{\mathcal{S}(\text{rx})} |y(\mathbf{q})|^2 d\mathbf{q}, \quad (22)$$

$$\mathbf{I}_2 = \int_{\mathcal{S}(\text{rx})} y^*(\mathbf{q}) \mathbf{E}^H d\mathbf{q}, \quad (23)$$

$$\mathbf{I}_3 = \int_{\mathcal{S}(\text{rx})} \mathbf{E}^* \mathbf{E}^H d\mathbf{q}. \quad (24)$$

Furthermore, by excluding constant value produced by \mathbf{I}_1 and adding a minus sign, we have

$$\mathcal{L}' = 2\Re \{ \mathbf{I}_2 \mathbf{P}^{-1} \mathbf{m} \} - \text{Tr} \{ \mathbf{I}_3 \mathbf{P}^{-1} \mathbf{m} \mathbf{m}^H (\mathbf{P}^{-1})^H \}. \quad (25)$$

Therefore, by maximizing (25), the position of the target can be identified. Specifically, for the single target scenario, (25) can be simplified to

$$\mathcal{L}' = \frac{\left(\int_{\mathcal{S}(\text{rx})} \tilde{E}^*(\mathbf{q}) y(\mathbf{q}) d\mathbf{q} \right)^2}{\int_{\mathcal{S}(\text{rx})} |\tilde{E}(\mathbf{q})|^2 d\mathbf{q}}. \quad (26)$$

Hence, the MLE spectrum can be obtained by traversing all possible \mathbf{r} [28]. The positions of the STs can be found at the spike locations on the MLE spectrum.

B. CRB Derivation for CAPAs

In this subsection, we characterize the sensing performance lower bound using CRB. To derive CRB, we first calculate the Fisher information matrix (FIM) for estimating $\boldsymbol{\xi}$, which is given by a partitioned matrix as:

$$\mathbf{J}_{\boldsymbol{\xi}} = \begin{bmatrix} \mathbf{J}_{\mathbf{r}\mathbf{r}} & \mathbf{J}_{\mathbf{r}\tilde{\boldsymbol{\alpha}}} \\ \mathbf{J}_{\mathbf{r}\tilde{\boldsymbol{\alpha}}}^T & \mathbf{J}_{\tilde{\boldsymbol{\alpha}}\tilde{\boldsymbol{\alpha}}} \end{bmatrix}. \quad (27)$$

According to [2], [14], each block matrix in FIM $\mathbf{J}_{\boldsymbol{\xi}}$ can be calculated according to

$$[\mathbf{J}_{\mathbf{r}\mathbf{r}}]_{m,n} = \frac{2}{\sigma^2} \int_{\mathcal{S}(\text{rx})} \Re \left\{ \frac{\partial E(\mathbf{q})}{\partial [\mathbf{r}]_m} \frac{\partial E^*(\mathbf{q})}{\partial [\mathbf{r}]_n} \right\} d\mathbf{q}, \quad (28)$$

$$[\mathbf{J}_{\mathbf{r}\tilde{\boldsymbol{\alpha}}}]_{m,n} = \frac{2}{\sigma^2} \int_{\mathcal{S}(\text{rx})} \Re \left\{ \frac{\partial E(\mathbf{q})}{\partial [\mathbf{r}]_m} \frac{\partial E^*(\mathbf{q})}{\partial [\tilde{\boldsymbol{\alpha}}]_n} \right\} d\mathbf{q}, \quad (29)$$

$$[\mathbf{J}_{\tilde{\boldsymbol{\alpha}}\tilde{\boldsymbol{\alpha}}}]_{m,n} = \frac{2}{\sigma^2} \int_{\mathcal{S}(\text{rx})} \Re \left\{ \frac{\partial E(\mathbf{q})}{\partial [\tilde{\boldsymbol{\alpha}}]_m} \frac{\partial E^*(\mathbf{q})}{\partial [\tilde{\boldsymbol{\alpha}}]_n} \right\} d\mathbf{q}, \quad (30)$$

where the expressions and derivations for \mathbf{J}_{rr} , $\mathbf{J}_{\text{r}\hat{\alpha}}$, and $\mathbf{J}_{\text{r}\hat{\alpha}}$ can be found in Appendix A. Following the above, the CRB matrix for estimating \mathbf{r} can be calculated according to

$$\text{CRB}(\mathbf{J}_{\text{rr}}) = [\mathbf{J}_{\text{rr}} - \mathbf{J}_{\text{r}\hat{\alpha}}\mathbf{J}_{\hat{\alpha}\hat{\alpha}}^{-1}\mathbf{J}_{\text{r}\hat{\alpha}}^{\text{T}}]^{-1}. \quad (31)$$

IV. CRB OPTIMIZATION

According to the CRB in (31), a mathematically tractable lower bound for sensing is established. Therefore, minimizing CRB under the unit-power constraint can elevate the sensing performance. Therefore, in this section, we first formulate the CRB minimization problem. Then, we propose an SMGD method to solve this problem with reduced complexity. Finally, a computational complexity analysis is attached.

A. Problem Formulation

Based on the derived CRB in (31), the optimization objective is to minimize CRB by designing a continuous source current function. By doing so, the sensing performance can be enhanced [29]. Here, we choose to minimize the trace of CRB, consistent with the approaches adopted for SPDA-enabled passive sensing scenarios, such as [29], [28], and [27]. Specifically, jointly considering the transmit power budget over the Tx P-CAPA, the CRB optimization problem can be formulated as

$$\begin{aligned} (\mathcal{P}_1) \quad & \min_{j(\mathbf{p})} \text{Tr} \{ \text{CRB}(\mathbf{J}_{\text{rr}}) \} \\ \text{s.t.} \quad & \int_{\mathcal{S}(\text{tx})} |J(\mathbf{p})|^2 d\mathbf{p} \leq P, \end{aligned} \quad (32a)$$

in which the optimization objective is to minimize the trace of CRB, while (32a) indicates that the total power of the source current over the entire Tx P-CAPA cannot exceed the given power budget P . Compared to conventional SPDAs [28], the crux of solving (\mathcal{P}_1) is to design a continuous function $\mathbf{J}(\mathbf{p})$ instead of finding a vector or matrix of discrete variables. Therefore, in the sequel, a lemma is first presented to identify the structure of the optimal solution and then followed by a Riemannian manifold algorithm to solve (\mathcal{P}_1) .

B. Structure of Optimal Solution

To make (\mathcal{P}_1) tractable, we prove that the optimal solution to (\mathcal{P}_1) lies within a sub-space spanned by the transmit responses. Therefore, the structure of the optimal solution is characterized by the following lemma:

Lemma 1. The optimal source current function $J(\mathbf{p})$ for (\mathcal{P}_1) can be expressed as a linear combination of transmit array responses, i.e.,

$$J(\mathbf{p}) = \sum_{n=1}^N w_n e^{jk_0 \|\mathbf{k}_n\|_2} = \mathbf{b}^{\text{T}} \mathbf{w}, \quad (37)$$

where the weights vector and basis vector can be respectively expressed as

$$\mathbf{w} = [w_1, w_2, \dots, w_N]^{\text{T}} \in \mathbb{C}^{N \times 1}, \quad (38)$$

$$\mathbf{b} = [e^{jk_0 \|\mathbf{k}_1\|_2}, \dots, e^{jk_0 \|\mathbf{k}_N\|_2}]^{\text{T}} \in \mathbb{C}^{N \times 1}. \quad (39)$$

Proof: Please refer to Appendix B. ■

Once the structure of the optimal solution is determined in light of **Lemma 1**, the rest is to determine the complex coefficient of each basis function, i.e., transmit array response. To do so, we extract the complex coefficient vector \mathbf{w} from the objective function and constraint of (\mathcal{P}_1) . As a preliminary step, the unit-power constraint presented by (32a) can be compactly expressed in a quadrature term, which is given by

$$\begin{aligned} \int_{\mathcal{S}(\text{tx})} |J(\mathbf{p})|^2 d\mathbf{p} &= \int_{\mathcal{S}(\text{tx})} |\mathbf{b}^{\text{T}} \mathbf{w}|^2 d\mathbf{p} \\ &= \int_{\mathcal{S}(\text{tx})} (\mathbf{w}^{\text{T}} \mathbf{b})^* \mathbf{b}^{\text{T}} \mathbf{w} d\mathbf{p} \\ &= \mathbf{w}^{\text{H}} \left(\int_{\mathcal{S}(\text{tx})} \mathbf{b}^* \mathbf{b}^{\text{T}} d\mathbf{p} \right) \mathbf{w} \\ &= \mathbf{w}^{\text{H}} \mathbf{B}_0 \mathbf{w} \leq P, \end{aligned} \quad (40)$$

where the entry of the cross integral matrix \mathbf{B}_0 can be expressed as

$$[\mathbf{B}_0]_{m,n} = \int_{\mathcal{S}(\text{tx})} e^{jk_0 \|\mathbf{k}_m\|_2} e^{-jk_0 \|\mathbf{k}_n\|_2} d\mathbf{p}. \quad (41)$$

In the sequel, we will analyze the expression of the objective function of (\mathcal{P}_1) . Before proceeding, we first define several terms for the clarity of presentation, which are shown at the top of the next page. Given $n = \{1, \dots, N\}$, $i = \{1, 2, 3\}$, and $j = \{1, 2\}$, the partial derivatives in Appendix A can be expressed as

$$\frac{\partial E(\mathbf{q})}{\partial [\xi]_m} = \begin{cases} \underbrace{\mathbf{g}_m^{\text{T}} \in \mathbb{C}^{N \times 1}}_{\substack{\left(h_{3,n}^{(i)} \mathbf{b}_{1,n}^{\text{T}} + h_{4,n} \mathbf{b}_{2,n,i}^{\text{T}} \right) \mathbf{w}, & \text{if } m = 3(n-1) + i \\ \underbrace{j^{i-1} h_{4,n}^{(i)} \mathbf{b}_{1,n} \mathbf{w}^{\text{T}}}_{\bar{\mathbf{g}}_m \in \mathbb{C}^{N \times 1}}, & \text{if } m = 3N + 2(n-1) + j \end{cases} \quad (42)$$

Therefore, we can further simplify the expression of the block matrix in the CRB expression as follows:

$$\begin{aligned} [\mathbf{J}_{\text{rr}}]_{m,n} &= \frac{2}{\sigma^2} \int_{\mathcal{S}(\text{rx})} \Re \left\{ (\mathbf{g}_m^{\text{T}} \mathbf{w})^* \mathbf{g}_n^{\text{T}} \mathbf{w} \right\} d\mathbf{q} \\ &= \frac{2}{\sigma^2} \Re \left\{ \int_{\mathcal{S}(\text{rx})} (\mathbf{w}^{\text{T}} \mathbf{g}_m)^* \mathbf{g}_n^{\text{T}} \mathbf{w} d\mathbf{q} \right\} \\ &= \frac{2}{\sigma^2} \Re \left\{ \int_{\mathcal{S}(\text{rx})} \mathbf{w}^{\text{H}} \mathbf{g}_m^* \mathbf{g}_n^{\text{T}} \mathbf{w} d\mathbf{q} \right\} \\ &= \frac{2}{\sigma^2} \Re \left\{ \mathbf{w}^{\text{H}} [\mathbf{B}_1]_{m,n} \mathbf{w} \right\} \\ &= \frac{2}{\sigma^2} \Re \left\{ \text{Tr} \left\{ \mathbf{w} \mathbf{w}^{\text{H}} [\mathbf{B}_1]_{m,n} \right\} \right\} \\ &= \frac{2}{\sigma^2} \Re \left\{ \text{Tr} \left\{ \mathbf{W} [\mathbf{B}_1]_{m,n} \right\} \right\}, \end{aligned} \quad (43)$$

where $\mathbf{W} \triangleq \mathbf{w} \mathbf{w}^{\text{H}}$ satisfied $\text{Rank} \{ \mathbf{W} \} = 1$. Thus, the entire \mathbf{J}_{rr} can be formulated as

$$\mathbf{J}_{\text{rr}} =$$

$$h_{1,n} \triangleq \int_{\mathcal{S}(\text{tx})} a_t(\mathbf{k}_n) \mathbf{b}^T \mathbf{w} d\mathbf{p} = \underbrace{\left[\int_{\mathcal{S}(\text{tx})} a_t(\mathbf{k}_n) [\mathbf{b}]_1 d\mathbf{p}, \dots, \int_{\mathcal{S}(\text{tx})} a_t(\mathbf{k}_n) [\mathbf{b}]_N d\mathbf{p} \right]}_{\triangleq \mathbf{b}_{1,n}^T \in \mathbb{C}^{N \times 1}} \mathbf{w} = \mathbf{b}_{1,n}^T \mathbf{w}, \quad (33)$$

$$\begin{aligned} h_{2,n}^{(i)} &\triangleq \int_{\mathcal{S}(\text{tx})} [\nabla_{\mathbf{r}_n} a_t(\mathbf{k}_n)]_i \mathbf{b}^T \mathbf{w} d\mathbf{p} \\ &= \underbrace{\left[\int_{\mathcal{S}(\text{tx})} [\nabla_{\mathbf{r}_n} a_t(\mathbf{k}_n)]_i [\mathbf{b}]_1 d\mathbf{p}, \dots, \int_{\mathcal{S}(\text{tx})} [\nabla_{\mathbf{r}_n} a_t(\mathbf{k}_n)]_i [\mathbf{b}]_N d\mathbf{p} \right]}_{\triangleq \mathbf{b}_{2,n,i}^T \in \mathbb{C}^{N \times 1}} \mathbf{w} = \mathbf{b}_{2,n,i}^T \mathbf{w}, \quad i \in \{1, 2, 3\}, \end{aligned} \quad (34)$$

$$h_{3,n}^{(i)} \triangleq c_0 \alpha_n [\nabla_{\mathbf{r}_n} a_r(\boldsymbol{\kappa}_n)]_i, \quad i \in \{1, 2, 3\}, \quad (35)$$

$$h_{4,n} \triangleq c_0 a_r(\boldsymbol{\kappa}_n) \alpha_n, \quad (36)$$

$$\begin{aligned} &\frac{2}{\sigma^2} \Re \left\{ \begin{bmatrix} \text{Tr} \{ \mathbf{W} [\mathbf{B}_1]_{1,1} \} & \cdots & \text{Tr} \{ \mathbf{W} [\mathbf{B}_1]_{3N,1} \} \\ \vdots & \ddots & \vdots \\ \text{Tr} \{ \mathbf{W} [\mathbf{B}_1]_{3N,1} \} & \cdots & \text{Tr} \{ \mathbf{W} [\mathbf{B}_1]_{3N,3N} \} \end{bmatrix} \right\} \\ &\triangleq \frac{2}{\sigma^2} \Re \{ (\mathbf{W} \otimes \mathbf{B}_1)^{\text{Tr}} \}, \end{aligned} \quad (44)$$

where \mathbf{B}_1 is a block matrix with entries $[\mathbf{B}_1]_{m,n} = \int_{\mathcal{S}(\text{rx})} \mathbf{g}_m^* \mathbf{g}_n^T d\mathbf{q}$ and \mathbf{A}^{Tr} denotes the blockwise trace operation of an arbitrary block matrix \mathbf{A} . With a similar method, the other partial matrices can be expressed as

$$\mathbf{J}_{\alpha\alpha} = \frac{2}{\sigma^2} \Re \{ (\mathbf{W} \otimes \mathbf{B}_2)^{\text{Tr}} \}, \quad (45)$$

$$\mathbf{J}_{\mathbf{r}\alpha} = \frac{2}{\sigma^2} \Re \{ (\mathbf{W} \otimes \mathbf{B}_3)^{\text{Tr}} \}, \quad (46)$$

where the cross-integral matrices are given by

$$[\mathbf{B}_2]_{m,n} = \int_{\mathcal{S}(\text{rx})} \bar{\mathbf{g}}_m^* \bar{\mathbf{g}}_n^T d\mathbf{q}, \quad (47)$$

$$[\mathbf{B}_3]_{m,n} = \int_{\mathcal{S}(\text{rx})} \mathbf{g}_m^* \bar{\mathbf{g}}_n^T d\mathbf{q}. \quad (48)$$

To calculate the integrals in CRB, we resort to the Gauss-Legendre numerical integral technique that can approximate an integral as a weighted summation. For simplicity, the implementation details of the Gauss-Legendre method are attached to Appendix C. Therefore, the optimization problem (\mathcal{P}_1) can be recast as

$$\begin{aligned} (\mathcal{P}_{1.1}) \quad \min_{\mathbf{w}} \quad &\frac{\sigma^2}{2} \text{Tr} \left\{ \Re \left\{ \left[(\mathbf{W} \otimes \mathbf{B}_1)^{\text{Tr}} \right. \right. \right. \\ &\left. \left. \left. - (\mathbf{W} \otimes \mathbf{B}_3)^{\text{Tr}} \left((\mathbf{W} \otimes \mathbf{B}_2)^{\text{Tr}} \right)^{-1} \left(\mathbf{W}^{\text{T}} \otimes \mathbf{B}_3^{\text{T}} \right)^{\text{Tr}} \right)^{-1} \right] \right\} \\ \text{s.t.} \quad &\text{Tr} \{ \mathbf{W} \mathbf{B}_0 \} \leq P, \end{aligned} \quad (49a)$$

$$\text{Rank} \{ \mathbf{W} \} = 1. \quad (49b)$$

C. SMGD Algorithm

To solve ($\mathcal{P}_{1.1}$), the most straightforward way is to resort to the semi-definite relaxation (SDR) method, which relaxes non-convex constraint (49b). Then, the rest of the problem is a convex problem that can be solved optimally using the standard CVX tools. Finally, the rank-one solution will

Algorithm 1: Armijo Backtracking Line Search

Input: Initial guess on step size v_0 , the current Riemannian gradient η , the former search direction \mathbf{d} , maximum allowed iteration T_{\max} , control parameter $c = 1 \times 10^{-4}$, objective function $F(\cdot)$, and shrinking parameter $\tau = 0.5$.

Output: Step size v .

- 1 Initialize the iteration counter $k = 0$;
- 2 **for** $k \leftarrow 0$ **to** T_{\max} **do**
- 3 **if** $F(\text{retr}_{\mathbf{w}} \{ \mathbf{w} + v_k \mathbf{d} \}) \leq F(\mathbf{w}) + cv_k \Re \{ \eta^H \mathbf{d} \}$ **then**
- 4 **break**;
- 4 **else** $v_k = \tau v_k$;
- 5 **end**
- 6 **if** $k = T_{\max}$ **then** $v = 1 \times 10^{-6}$;
- 7 **else** $v = v_k$;
- 8 **return** *The optimized step size* v .

be recovered from \mathbf{W} using eigenvalue decomposition and Gaussian randomization procedure. However, the optimality of the obtained rank-one solution cannot be guaranteed, and it introduces high computational complexity. Therefore, we adopt the Riemannian manifold optimization method to solve ($\mathcal{P}_{1.1}$), whose superiority over the SDR method will be demonstrated in the analysis of the computational complex and the simulation section.

To adopt the SMGD method, we first release the rank-one constraint (49b) by treating \mathbf{W} as a vector multiplication, i.e., $\mathbf{w} \mathbf{w}^H$. Therefore, by optimizing $\mathbf{w} \in \mathbb{C}^{N \times 1}$, we can guarantee to obtain a rank-one solution. Then, we deal with the power constraint (49a). The optimal solution is obtained at the boundary of (49a). This can be proven using proof by contradiction, as a better solution can always be achieved by increasing the power until the boundary condition is met. In this case, constraint (49a) can be converted into a unit-power constraint represented by

$$\mathbf{w}^H \mathbf{B}_0 \mathbf{w} = P. \quad (50)$$

Given $\mathbf{B}_0 \in \mathbb{S}_{++}^N$ is a positive-defined matrix, (50) defines a complex ellipse manifold denoted by \mathcal{M} , by optimizing on which the unit power constraint can be released. For the simplicity of presentation, we denote the objective function of ($\mathcal{P}_{1.1}$) as $F(\mathbf{w})$. Hence, the original optimization problem can

be recast as

$$(\mathcal{P}_{1.2}) \quad \mathbf{w} = \arg \min_{\mathbf{w} \in \mathcal{M}} F(\mathbf{w}), \quad (51a)$$

which is an unconstrained optimization on a manifold and can be solved efficiently by gradient descent. To enable the gradient-descent-based method on the manifold \mathcal{M} , we must first define the gradients on manifold \mathcal{M} , which represent the direction of the steepest increase of a function. As a prerequisite step, the inner product between two vectors, $\langle \cdot, \cdot \rangle$ on \mathcal{M} , can be evaluated as

$$\langle \mathbf{u}, \mathbf{v} \rangle = \mathbf{u}^H \mathbf{B}_0 \mathbf{v}. \quad (52)$$

where \mathbf{u} and \mathbf{v} are two points on the manifold \mathcal{M} . Thus, \mathcal{M} becomes a Riemannian manifold. According to [30] and [31], each step of the gradient descent methods in the Euclidean space has its corresponding counterpart on the Riemannian manifold. For a given point \mathbf{w} on \mathcal{M} , the tangent space is defined by

$$\mathcal{T}_{\mathbf{w}} \mathcal{M} \triangleq \{ \boldsymbol{\eta} \in \mathbb{C}^{N \times 1} : \Re \{ \mathbf{w}^H \mathbf{B}_0 \boldsymbol{\eta} \} = 0 \}, \quad (53)$$

which describes a vector set perpendicular to \mathbf{w} . Then, the Riemannian gradient defined by the steepest direction on \mathcal{M} can be expressed by

$$\text{grad}_{\mathbf{w}} \{ F(\mathbf{w}) \} = \nabla_{\mathbf{w}} F(\mathbf{w}) - \frac{\mathbf{w}^H \mathbf{B}_0 \nabla_{\mathbf{w}} F(\mathbf{w})}{\mathbf{w}^H \mathbf{B}_0 \mathbf{w}} \mathbf{B}_0 \mathbf{w} = \boldsymbol{\eta}, \quad (54)$$

which can be geometrically interpreted as the maximum projection of the Euclidean gradient $\nabla_{\mathbf{w}} F(\mathbf{w})$ to manifold \mathcal{M} . The derivations of $\nabla_{\mathbf{w}} F(\mathbf{w})$ can be obtained by applying a simplified chain rule for complex-valued variables in real-valued functions [32], which is omitted here for brevity. Then, a search direction is defined by $v\mathbf{d}$, denoting a step of size $v > 0$. According to the Fletcher-Reeves (FR) method, the search direction can be specified by

$$\mathbf{d}^+ = -\boldsymbol{\eta}^+ + \frac{\|\boldsymbol{\eta}^+\|_2^2}{\|\boldsymbol{\eta}^-\|_2^2} \mathbf{d}^-, \quad (55)$$

the superscripts $+$ and $-$ denote the current and the previous iteration, respectively. To enhance the algorithm's robustness, we utilize the Armijo backtracking line search algorithm summarized in **Algorithm 1** to find the optimal v at each iteration. Furthermore, to ensure that the destination of $v\mathbf{d}$ is on the manifold \mathcal{M} , we define the retraction operator, that is characterized by

$$\text{retr}_{\mathbf{w}} \{ \mathbf{w} + v\mathbf{d} \} \triangleq \frac{\mathbf{w} + v\mathbf{d}}{\sqrt{\Re \{ (\mathbf{w} + v\mathbf{d})^H \mathbf{B}_0 (\mathbf{w} + v\mathbf{d}) \}}}. \quad (56)$$

Besides, to adopt the conjugated gradient method on \mathcal{M} , we must define a transport operation that maps two directions of two different tangent spaces. This operation is distinguished by

$$\text{trans}_{\mathbf{w}^- \rightarrow \mathbf{w}^+} \{ \mathbf{d}^- \} = \mathbf{d}^+, \quad (57)$$

where \mathbf{w}^+ and \mathbf{w}^- are the point at the current and the former iteration, respectively. Thus, the overall algorithm is

Algorithm 2: SMGD Algorithm for CRB Minimizing

Input: Initial guess of weight vector \mathbf{w}_0 , Rx/Tx CAPA coordinate sets $\mathcal{S}^{(\text{rx})}$ and $\mathcal{S}^{(\text{tx})}$, basis functions for STs, noise power σ^2 , the number of points along the x - and y -axes N_x and N_y , error-tolerant threshold δ , maximum number of iterations T_{\max} .

Output: The optimized weight vector \mathbf{w} .

// Prerequisite Step:

- 1 Calculate the initial gradient descent direction via $\mathbf{d}_0 = -\text{grad}_{\mathbf{w}} \{ F(\mathbf{w}_0) \}$ according to (54) and initialize $k = 0$;
 - // Performing Conjugate Gradient Descent:
 - 2 **while** $\|\mathbf{d}_{k+1} - \mathbf{d}_k\|_2 \geq \delta$ and $k < T_{\max}$ **do**
 - 3 Find the step size v_k by **Algorithm 1**;
 - 4 Find the next point \mathbf{w}_{k+1} via retraction $\mathbf{w}_{k+1} = \text{retr}_{\mathbf{w}} \{ \mathbf{w}_k + v_k \mathbf{d}_k \}$ according to (56);
 - 5 Compute the Riemannian gradient at point \mathbf{w}_{k+1} via $\boldsymbol{\eta}_{k+1} = \text{grad}_{\mathbf{w}} \{ F(\mathbf{w}_{k+1}) \}$;
 - 6 Update the search direction via (55) and transport this direction via (57);
 - 7 Step into the next iteration by $k = k + 1$;
 - 8 **end**
 - 9 **return** The optimized weight vector $\mathbf{w} = \mathbf{w}_k$.
-

summarized in **Algorithm 2**.

D. Analysis of Computation Complexity

Given the number of targets is N , the computational complexity for calculating the Euclidean gradient, Riemannian gradient, retraction operation, and transport operation is $\mathcal{O}(N^2)$. Then, the complexity of the line searching is $\mathcal{O}(NT_{\max})$. Therefore, the overall computational complexity for one iteration is given by $\mathcal{O}(N^2 + NT_{\max})$. As a comparison, according to [33], the per-iteration complexity of the SDR algorithm is $\mathcal{O}(N^{4.5})$. It is important to note that the computational complexity of recovering the rank-1 structure is excluded in this analysis, as including it would further increase the complexity of the SDR algorithm. Hence, the proposed algorithm has much lower complexity than the SDR approach. The convergence behavior of the proposed algorithm will be discussed in the upcoming section.

V. NUMERICAL RESULTS

In this section, numerical results are presented to evaluate the performance of the proposed SMGD algorithm and to analyze the performance of the CAPA-based NISE systems. The parameter settings are listed in Table I and utilized throughout all the simulations unless otherwise specified. For the proposed SMGD algorithm, we set the initial step size as $v_0 = 1.0$, the control parameter as $c = 1 \times 10^{-4}$, and the shrinking parameters $\tau = 0.5$, respectively

A. Convergence of the Proposed SMGD Algorithm

In Fig. 3, we examine the convergence performance of the proposed SMGD method in comparison to multiple benchmarks: 1) the SDR method with Gaussian randomization recovering, referred to as ‘‘SDR’’, 2) the plain conjugated gradient descent method on the manifold, referred to as ‘‘Plain’’, and 3) the Polak-Ribiere-based conjugated gradient descent method on the manifold, referred to as ‘‘PR’’, respectively.

TABLE I: System Parameters

N	The number of sensing targets	2	f	The carrier frequency	28 GHz
$W_{\min}^{(\text{tx})}$	The lower boundary of Tx CAPA's width	-1 m	$W_{\max}^{(\text{tx})}$	The upper boundary of Tx CAPA's width	0 m
$H_{\min}^{(\text{tx})}$	The lower boundary of Tx CAPA's height	-0.5 m	$H_{\max}^{(\text{tx})}$	The upper boundary of Tx CAPA's height	0.5 m
$W_{\min}^{(\text{rx})}$	The lower boundary of Rx CAPA's width	0 m	$W_{\max}^{(\text{rx})}$	The upper boundary of Rx CAPA's width	1 m
$H_{\min}^{(\text{rx})}$	The lower boundary of Rx CAPA's height	-0.5 m	$H_{\max}^{(\text{rx})}$	The upper boundary of Rx CAPA's height	0.5 m
P	The transmit Power Tx CAPA	100 mA ²	σ^2	The noise power at Rx CAPA	5.6×10^{-3} V ² /m ²
\mathbf{r}_1	The position of the first ST	$[-5.0, 0.0, +5.0]$ m	\mathbf{r}_2	The position of the second ST	$[+5.0, 0.0, +5.0]$ m
N_x/N_y	The number of GL points	300	α_n	The reflection coefficient of the n -th ST	$10 + 10j$
η_0	The intrinsic impedance	376.73 Ω			

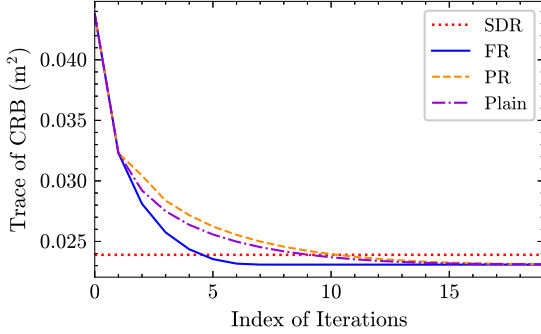


Fig. 3: An illustration of the convergence behavior of SMGD Algorithm over 100 Monte Carlo simulations.

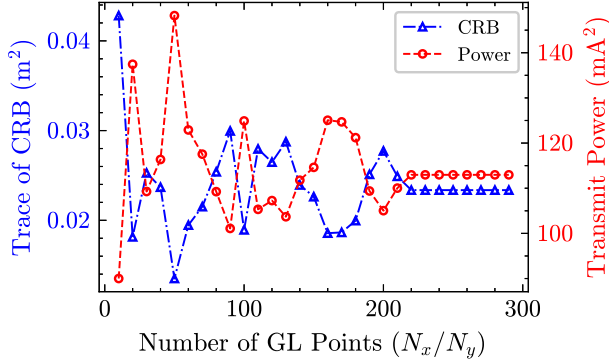
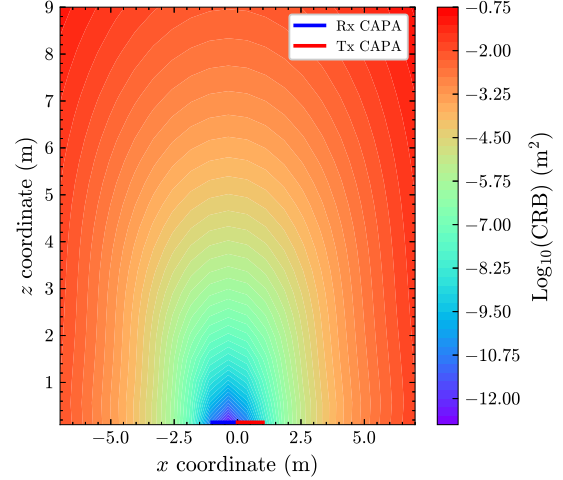


Fig. 4: An illustration of the convergence behavior of Gaussian-Legendre (GL) numerical integral.

It is noted that the convergence behavior of “SDR” is not shown here due to the large number of iterations needed for both the interior-point method and Gaussian randomization procedure for rank-1 recovery. Instead, the horizontal line of “SDR” represents its averaged converged value, serving as a performance bound at the cost of high computational complexity. As observed in Fig. 3, both the “FR” and “PR” methods outperform the plain implementation of conjugated gradient descent, i.e., “Plain”. In addition, “FR” can converge more quickly compared to “PR”, thereby making it a more favorable choice for our problem. More importantly, “FR” can obtain a close performance to that of “SDR” with a small number of iterations and reduced complexity.

In Fig. 4, we present the convergence behavior of GL numerical integration by fixing coefficient vector \mathbf{w} as a random complex-valued vector, that does not necessarily obey the unit-power constraint. It can be seen that when N_x/N_y

Fig. 5: An illustration of achieved CRB over the XOZ plane.

exceeds 220, the values of integral terms for both CRB and transmit power converge to fixed values, thereby justifying our setting for N_x and N_y in Table I. In contrast to the communication-only [18] and active sensing scenarios [2], the integrations require more GL points for convergence. This can be attributed to the four-dimensional (4D) rather than two-dimensional (2D) integrations involved in CRB calculation.

B. Evaluation of MLE and Beam Pattern

Fig. 5 illustrates the achieved CRB over the XOZ plane. Specifically, a single ST is placed on a grid with 400 points over an area of $[-7 \text{ m}, +7 \text{ m}] \times [0.1 \text{ m}, 9 \text{ m}]$. In addition, we utilize $\log_{10}\{\cdot\}$ function to post-process the achieved CRB. The results reveal that: 1) as ST moves closer to the Rx P-CAPA, a lower CRB is achieved, indicating an improved positioning accuracy, and 2) the CRB distribution is symmetric concerning the center point of the Rx P-CAPA.

Moreover, we present the MLE spectrum for the single ST scenarios, specifically for “ST2” at \mathbf{r}_2 exists. Using the derivations in Section III-A, the MLE spectrum along x - and z -axes are depicted by Fig. 6. To provide a comparison, we also present a random policy, in which source current is generated according to

$$J(\mathbf{p}) = \frac{1}{\sqrt{|\mathcal{S}^{(\text{tx})}|}} \exp\{j \text{Uniform}(-\pi, +\pi)\},$$

where $\text{Uniform}(-\pi, +\pi)$ can generate samples according to a uniform distribution in a range of $[-\pi, +\pi]$. As demonstrated

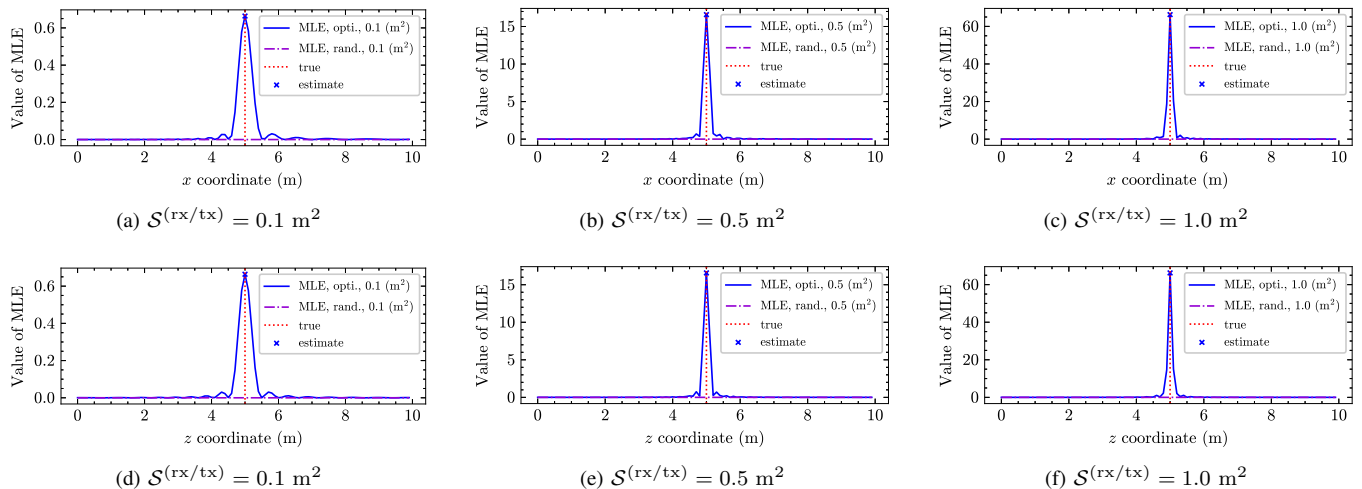


Fig. 6: An illustration of the MLE spectrum along the x - and z -axes, respectively. “opti.” and “rand.” represent the proposed optimization method and the random policy, respectively.

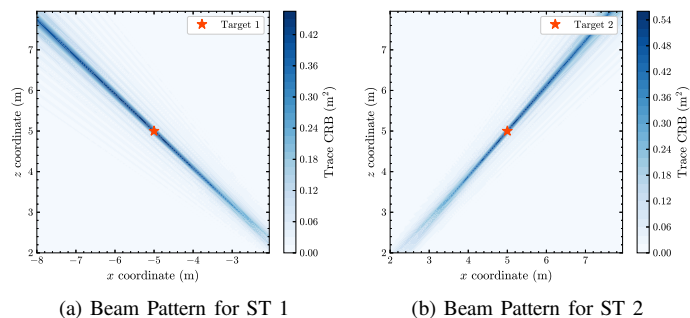


Fig. 7: An illustration of beam pattern for ST 1 at $[-5 \text{ m}, 0 \text{ m}, +5 \text{ m}]$ and ST 2 at $[+5 \text{ m}, 0 \text{ m}, +5 \text{ m}]$, respectively.

by Fig. 6, the proposed method significantly outperforms the random policy, demonstrating its effectiveness in enhancing sensing accuracy. From these sub-figures, it can be observed that, due to the dependence of the EM-based channel model on both x and z coordinates, CAPA-enabled NISE achieves a two-dimensional positioning, in contrast to the angle-only sensing in the conventional far-field scenarios. More importantly, as the area of Tx and Rx P-CAPA increases, the spike in the MLE spectrum becomes sharper and taller with reduced side lobe amplitudes. This trend indicates that increasing the CAPA size enhances positioning accuracy.

For the multi-ST scenario, the MLE calculation is high-dimensional, making it hard to visualize directly. As an alternative, we present the beam pattern, following the methodology outlined in [34]. It is noteworthy that the path loss is eliminated in beam pattern calculations to remove the impact of distance on the results. With these preliminaries, the beam patterns for ST 1 and ST 2 are depicted in Fig. 7. As shown in this figure, the energy of the beams is concentrated at the respective locations of ST 1 and ST 2, demonstrating the effectiveness of the proposed algorithm in the multi-ST scenario.

C. Evaluation of CRB

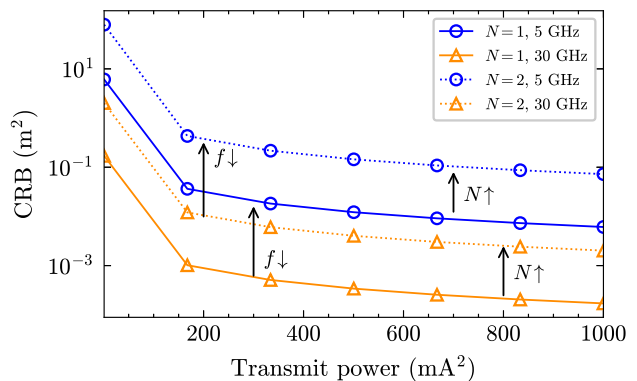


Fig. 8: An illustration of the achieved CRB versus transmit power under different numbers of target N and carrier frequency f .

1) *CRB Versus Carrier Frequency*: In Fig. 8, we analyze the achieved CRB as a function of transmit power under different numbers of the target N and carrier frequency f . From this figure, it can be observed that: 1) As the transmit power increases, the CRB decreases correspondingly, aligning well with the conclusions drawn for the SPDA-based near-field sensing scenarios. 2) As carrier frequency increases, a further reduction in CRB is observed, indicating an improved sensing accuracy; 3) As more STs need to be positioned, the total CRB worsens, which can be attributed to the allocation of a limited total power budget, thus reducing the sensing accuracy for each target.

2) *Comparison Between CAPAs and SPDAs*: In Fig. 9, we compare the investigated CAPA system to the conventional SPDA system to underscore the superiority of continuous aperture (CA). The conventional SPDA system is analyzed by sampling the Rx and Tx antenna planes with $d = \frac{\lambda}{2}$ as spacing and $A_d = \frac{\lambda^2}{4\pi}$ as the effective aperture areas of each antenna. The results demonstrate that the achieved CRB decreases as carrier frequency increases, thus reinforcing the results presented in Fig. 8. Moreover, compared to the conventional SPDA setup, the CAPA-based NISE achieves an order-of-

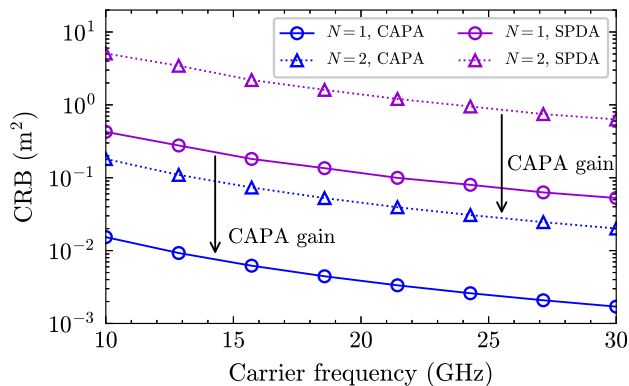


Fig. 9: An illustration of the achieved CRB versus carrier frequency f under different types of antenna architecture, i.e., CAPA and SPDA.

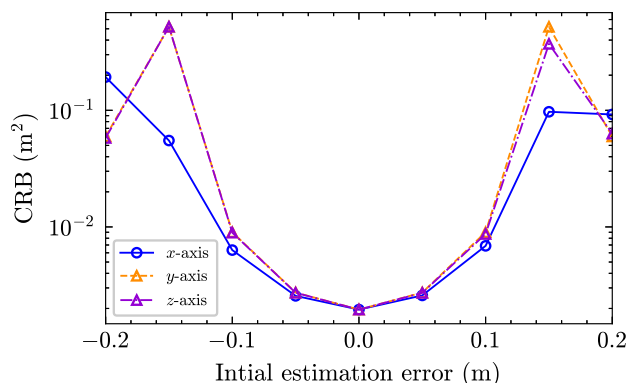


Fig. 10: An illustration of the robustness of CRB optimization to initial position estimation results along x -, y -, z -axes for ST 1.

magnitude improvement in accuracy, thereby underscoring the advantages of continuous aperture arrays. Lastly, as the number of STs increases, the CRB also increases as depicted in Fig. 8.

3) *CRB Versus Initial Estimation Error*: As highlighted in the pioneering work on CRB optimization [29], CRB optimization requires prior knowledge of the target's position. Therefore, it is essential to evaluate the robustness of the proposed algorithm to errors in the initial position estimation. Fig. 10 illustrates the achieved CRB as a function of the initial estimation error. The results indicate that the CRB does not increase significantly when the error is within the range of $[-0.15 \text{ m}, 0.15 \text{ m}]$, demonstrating the robustness of the algorithm in this range. It is important to note that since the target is located at $\mathbf{r}_1 = [-5.0 \text{ m}, 0.0 \text{ m}, 5.0 \text{ m}]$, and the Rx-CAPA center is at $[-5.0 \text{ m}, 0.0 \text{ m}, 5.0 \text{ m}]$, the error is symmetric only along the y -axis. This symmetry is further validated by the symmetric property of the CRB observed in Fig. 5.

VI. CONCLUSIONS

This paper proposed a CRB minimization framework for CAPA-enabled NISE systems. Specifically, different from existing research on active sensing with CAPA, the CRB expression was derived for a more practical passive sensing setup. Based on the derivation, the CRB minimization problem was formulated, by solving which the sensing accuracy can be

enhanced. To make the optimization of the continuous source current function tractable, the structure of the optimal solution was proved, followed by the SMGD algorithm developed to obtain the coefficient vector with reduced computational complexity. The numerical results verified the effectiveness of the proposed SMGD method and demonstrated the superiority of CAPAs over conventional SPDAs in terms of sensing performance.

APPENDIX A THE DERIVATIONS OF CRB IN (31)

In light of [2], [29], [35], the expression for the (m, n) -th entry in $\mathbf{J}_{\mathbf{r}\mathbf{r}}$ can be expressed as

$$\begin{aligned} [\mathbf{J}_{\mathbf{r}\mathbf{r}}]_{m,n} &= \frac{2}{\sigma^2} \int_{\mathcal{S}^{(\text{rx})}} \Re \left\{ \frac{\partial E(\mathbf{q})}{\partial [\mathbf{r}]_m} \frac{\partial E^*(\mathbf{q})}{\partial [\mathbf{r}]_n} \right\} d\mathbf{q} \\ &= \frac{2}{\sigma^2} \int_{H_{\min}^{(\text{rx})}}^{H_{\max}^{(\text{rx})}} \int_{W_{\min}^{(\text{rx})}}^{W_{\max}^{(\text{rx})}} \Re \left\{ \frac{\partial E(x, y)}{\partial [\mathbf{r}]_m} \frac{\partial E^*(x, y)}{\partial [\mathbf{r}]_n} \right\} dx dy. \end{aligned} \quad (\text{A-1})$$

It is noted that, since both the Tx and Rx CAPAs are placed on the XOY plane, we define $E(x, y) \triangleq E(\mathbf{q})|_{z=0}$ in (A-1). Then, based on (13) and (8), we can factor out the summation term through

$$\begin{aligned} E(\mathbf{q}) &\triangleq \int_{\mathcal{S}^{(\text{tx})}} h(\mathbf{q}, \mathbf{p}) J(\mathbf{p}) d\mathbf{p} \\ &= c_0 \int_{\mathcal{S}^{(\text{tx})}} \sum_{n=1}^N a_r(\boldsymbol{\kappa}_n) \alpha_n a_t(\mathbf{k}_n) J(\mathbf{p}) d\mathbf{p} \\ &\stackrel{(a)}{=} c_0 \sum_{n=1}^N \int_{\mathcal{S}^{(\text{tx})}} a_r(\boldsymbol{\kappa}_n) \alpha_n a_t(\mathbf{k}_n) J(\mathbf{p}) d\mathbf{p} \\ &\stackrel{(b)}{=} c_0 \sum_{n=1}^N a_r(\boldsymbol{\kappa}_n) \alpha_n \int_{\mathcal{S}^{(\text{tx})}} a_t(\mathbf{k}_n) J(\mathbf{p}) d\mathbf{p}, \end{aligned}$$

where (a) is obtained by leveraging the linear property of integration, and (b) is derived by extracting the terms independent to \mathbf{p} . Following this, the partial derivative of $E(\mathbf{q})$ with respect to \mathbf{r} can be computed. In particular, for the n -th ST where $n \in \mathcal{N}$, the partial derivative with respect to \mathbf{r}_n can be calculated via

$$\begin{aligned} \nabla_{\mathbf{r}_n} E(\mathbf{q}) &= \nabla_{\mathbf{r}_n} \left\{ c_0 a_r(\boldsymbol{\kappa}_n) \alpha_n \int_{\mathcal{S}^{(\text{tx})}} a_t(\mathbf{k}_n) J(\mathbf{p}) d\mathbf{p} \right\} \\ &= c_0 \alpha_n \nabla_{\mathbf{r}_n} a_r(\boldsymbol{\kappa}_n) \int_{\mathcal{S}^{(\text{tx})}} a_t(\mathbf{k}_n) J(\mathbf{p}) d\mathbf{p} \\ &\quad + c_0 a_r(\boldsymbol{\kappa}_n) \alpha_n \int_{\mathcal{S}^{(\text{tx})}} \nabla_{\mathbf{r}_n} a_t(\mathbf{k}_n) J(\mathbf{p}) d\mathbf{p}, \end{aligned} \quad (\text{A-2})$$

in which $\nabla_{\mathbf{r}_n} a_t(\mathbf{k}_n)$ and $\nabla_{\mathbf{r}_n} a_r(\boldsymbol{\kappa}_n)$ can be derived as

$$\begin{aligned} \nabla_{\mathbf{r}_n} a_t(\mathbf{k}_n) &= \nabla_{\mathbf{r}_n} \left\{ \frac{1}{\|\mathbf{k}_n\|_2} e^{-jk_0 \|\mathbf{k}_n\|_2} \right\} \\ &= -\frac{\mathbf{r}_n}{\|\mathbf{k}_n\|_2^3} (1 + jk_0 \|\mathbf{k}_n\|_2) e^{-jk_0 \|\mathbf{k}_n\|_2}, \quad (\text{A-3}) \\ \nabla_{\mathbf{r}_n} a_r(\boldsymbol{\kappa}_n) &= \nabla_{\mathbf{r}_n} \left\{ \frac{1}{\|\boldsymbol{\kappa}_n\|_2} e^{jk_0 \|\boldsymbol{\kappa}_n\|_2} \right\} \end{aligned}$$

$$= \frac{\mathbf{r}_n}{\|\mathbf{k}_n\|_2^3} (1 - j k_0 \|\mathbf{k}_n\|_2) e^{j k_0 \|\mathbf{k}_n\|_2}. \quad (\text{A-4})$$

Similarly, the (m, n) -th entry in $\mathbf{J}_{\alpha\alpha}$ we have

$$[\mathbf{J}_{\alpha\alpha}]_{m,n} = \int_{H_{\min}^{(\text{rx})}}^{H_{\max}^{(\text{rx})}} \int_{W_{\min}^{(\text{rx})}}^{W_{\max}^{(\text{rx})}} \Re \left\{ \frac{\partial E(x, y)}{\partial [\alpha]_m} \frac{\partial E^*(x, y)}{\partial [\alpha]_n} \right\} dx dy, \quad (\text{A-5})$$

where the integrands are specified by

$$\frac{\partial E(\mathbf{q})}{\partial \Re\{\alpha_n\}} = c_0 a_r(\mathbf{k}_n) \int_{\mathcal{S}^{(\text{tx})}} a_t(\mathbf{k}_n) J(\mathbf{p}) d\mathbf{p}, \quad (\text{A-6})$$

$$\frac{\partial E(\mathbf{q})}{\partial \Im\{\alpha_n\}} = j c_0 a_r(\mathbf{k}_n) \int_{\mathcal{S}^{(\text{tx})}} a_t(\mathbf{k}_n) J(\mathbf{p}) d\mathbf{p}. \quad (\text{A-7})$$

Finally, the (m, n) -th entries in $\mathbf{J}_{\mathbf{r}\alpha}$ is defined by

$$[\mathbf{J}_{\mathbf{r}\alpha}]_{m,n} = \int_{H_{\min}^{(\text{rx})}}^{H_{\max}^{(\text{rx})}} \int_{W_{\min}^{(\text{rx})}}^{W_{\max}^{(\text{rx})}} \Re \left\{ \frac{\partial E(x, y)}{\partial [\mathbf{r}]_m} \frac{\partial E^*(x, y)}{\partial [\alpha]_n} \right\} dx dy, \quad (\text{A-8})$$

where the integrands can be found in (A-2), (A-6), and (A-7).

APPENDIX B PROOF OF LEMMA 1

To prove this lemma, we need to illustrate all the optimal solutions are located in the subspace V spanned a set of basis functions (or the transmit array responses) $\mathcal{B} = \{e^{j k_0 \|\mathbf{k}_n\|_2}\}_{n \in \mathcal{N}}$. Inspired by [36], we utilize proof by contradiction.

First, we assume that an optimal solution $J^{\text{opt.}}(\mathbf{p})$ to (\mathcal{P}_1) can be found outside the subspace V . Therefore, $J^{\text{opt.}}(\mathbf{p})$ can be expressed by a component that is parallel to V and a component that is perpendicular to V , thereby yielding

$$J^{\text{opt.}}(\mathbf{p}) = J_{\perp}(\mathbf{p}) + J_{\parallel}(\mathbf{p}), \quad (\text{B-1})$$

where the perpendicular component $J_{\perp}(\mathbf{p})$ satisfies

$$\begin{aligned} & \langle e^{j k_0 \|\mathbf{k}_n\|_2}, J_{\perp}(\mathbf{p}) \rangle \\ &= \int_{\mathcal{S}^{(\text{tx})}} e^{j k_0 \|\mathbf{k}_n\|_2} J_{\perp}(\mathbf{p}) d\mathbf{p} = 0. \text{ for } \forall n \in \mathcal{N}, \end{aligned} \quad (\text{B-2})$$

Then, we calculate the trace of CRB when $J^{\text{opt.}}(\mathbf{p})$ is utilized for transmission. In light of (A-2), (A-6), and (A-7), the following terms related to $J^{\text{opt.}}(\mathbf{p})$ can be simplified by

$$\begin{aligned} I_{1,n} &= \int_{\mathcal{S}^{(\text{tx})}} a_t(\mathbf{k}_n) J^{\text{opt.}}(\mathbf{p}) d\mathbf{p} \\ &= \int_{\mathcal{S}^{(\text{tx})}} a_t(\mathbf{k}_n) J_{\parallel}(\mathbf{p}) d\mathbf{p}, \quad \text{for } n \in \mathcal{N} \\ I_{2,n} &= \int_{\mathcal{S}^{(\text{tx})}} \nabla_{\mathbf{r}_n} a_t(\mathbf{k}_n) J^{\text{opt.}}(\mathbf{p}) d\mathbf{p} \\ &= \int_{\mathcal{S}^{(\text{tx})}} \nabla_{\mathbf{r}_n} a_t(\mathbf{k}_n) J_{\parallel}(\mathbf{p}) d\mathbf{p}, \text{ for } n \in \mathcal{N} \end{aligned}$$

where the orthogonality in (B-2) is utilized to cancel out the terms containing $J_{\perp}(\mathbf{p})$. It can be observed that the perpendicular component $J_{\perp}(\mathbf{p})$ has no contributions to the trace of CRB. Therefore, we can construct a better solution by

concentrating power on the parallel component $J_{\parallel}(\mathbf{p})$. Jointly considering the power budget, the new solution is given by

$$\begin{aligned} J'(\mathbf{p}) &= \sqrt{\frac{P}{\int_{\mathcal{S}^{(\text{tx})}} |J_{\parallel}(\mathbf{p})|^2 d\mathbf{p}}} J_{\parallel}(\mathbf{p}) \\ &= \sqrt{\frac{\int_{\mathcal{S}^{(\text{tx})}} |J^{\text{opt.}}(\mathbf{p})|^2 d\mathbf{p}}{\int_{\mathcal{S}^{(\text{tx})}} |J_{\parallel}(\mathbf{p})|^2 d\mathbf{p}}} J_{\parallel}(\mathbf{p}) = \sqrt{c_1} J_{\parallel}(\mathbf{p}) \end{aligned}$$

By capitalizing on the orthogonality, we have the following derivations:

$$\begin{aligned} \int_{\mathcal{S}^{(\text{tx})}} |J^{\text{opt.}}(\mathbf{p})|^2 d\mathbf{p} &= \int_{\mathcal{S}^{(\text{tx})}} |J_{\perp}(\mathbf{p}) + J_{\parallel}(\mathbf{p})|^2 d\mathbf{p} \\ &= \int_{\mathcal{S}^{(\text{tx})}} |J_{\perp}(\mathbf{p})|^2 d\mathbf{p} + \int_{\mathcal{S}^{(\text{tx})}} |J_{\parallel}(\mathbf{p})|^2 d\mathbf{p} \\ &> \int_{\mathcal{S}^{(\text{tx})}} |J_{\parallel}(\mathbf{p})|^2 d\mathbf{p}. \end{aligned} \quad (\text{B-3})$$

According to (B-3), we have $c_1 > 1$. Then, by substituting $J_{\parallel}(\mathbf{p})$ with $J'(\mathbf{p})$, we have

$$I'_{1,n} = \sqrt{c_1} I_{1,n}, \quad I'_{2,n} = \sqrt{c_1} I_{2,n}, \quad \text{for } \forall n \in \mathcal{N}.$$

Due to $\sqrt{c_1}$ being a constant number and irrelevant to the outer integral over $\mathcal{S}^{(\text{tx})}$, we therefore have $\mathbf{J}'_{\mathbf{r}\mathbf{r}} = c_1 \mathbf{J}_{\mathbf{r}\mathbf{r}}$, $\mathbf{J}'_{\mathbf{r}\alpha} = c_1 \mathbf{J}_{\mathbf{r}\alpha}$, and $\mathbf{J}'_{\alpha\alpha} = c_1 \mathbf{J}_{\alpha\alpha}$, where $\mathbf{J}_{\mathbf{r}\mathbf{r}}$, $\mathbf{J}_{\mathbf{r}\alpha}$, and $\mathbf{J}_{\alpha\alpha}$ are the partial FIM matrices parameterized by $J_{\parallel}(\mathbf{p})$ (or equivalently $J^{\text{opt.}}(\mathbf{p})$). Hence, we have the following inequality holds:

$$\begin{aligned} \mathbf{J}'_{\mathbf{r}\mathbf{r}} - \mathbf{J}'_{\mathbf{r}\alpha} (\mathbf{J}'_{\alpha\alpha})^{-1} (\mathbf{J}'_{\mathbf{r}\alpha})^T &= c_1 (\mathbf{J}_{\mathbf{r}\mathbf{r}} - \mathbf{J}_{\mathbf{r}\alpha} \mathbf{J}_{\alpha\alpha}^{-1} \mathbf{J}_{\mathbf{r}\alpha}^T) \\ &> \mathbf{J}_{\mathbf{r}\mathbf{r}} - \mathbf{J}_{\mathbf{r}\alpha} \mathbf{J}_{\alpha\alpha}^{-1} \mathbf{J}_{\mathbf{r}\alpha}^T. \end{aligned}$$

Since $\text{Tr}\{(\cdot)^{-1}\}$ is a decreasing function over semidefinite matrix space, we have

$$\text{Tr}\{\text{CRB}(\mathbf{J}'_{\mathbf{r}\mathbf{r}})\} < \text{Tr}\{\text{CRB}(\mathbf{J}_{\mathbf{r}\mathbf{r}})\},$$

which indicates that we find a better solution by constructing $J'(\mathbf{p})$. In this case, $J^{\text{opt.}}(\mathbf{p})$ is not the optimal solution, which contradicts the initial assumption on $J^{\text{opt.}}(\mathbf{p})$. Consequently, the optimal solution only contains the component parallel to the subspace V .

APPENDIX C IMPLEMENTATION OF GAUSS-LEGENDRE NUMERICAL INTEGRAL

Letting the integrand be $f(x, y)$, we have the following derivations by performing a change of interval:

$$\begin{aligned} I &= \int_{\underline{H}}^{\overline{H}} \int_{\underline{W}}^{\overline{W}} f(x, y) dx dy \\ &= \int_{-1}^1 \int_{-1}^1 f(c_x x' + b_x, c_y y' + b_y) c_x c_y dx' dy', \end{aligned} \quad (\text{C-1})$$

where $x = c_x x' + b_x$ with $c_x \triangleq 0.5(\overline{W} - \underline{W})$ and $b_x \triangleq 0.5(\overline{W} + \underline{W})$, and $y = c_y y' + b_y$ with $c_y \triangleq 0.5(\overline{H} - \underline{H})$ and $b_y \triangleq 0.5(\overline{H} + \underline{H})$, respectively. Based on where the integral is carried out, i.e., either on the Tx or Rx CAPAs, we select the following parameters accordingly: $\overline{W} = \{W_{\max}^{(\text{rx})}, W_{\max}^{(\text{tx})}\}$, $\underline{W} = \{W_{\min}^{(\text{rx})}, W_{\min}^{(\text{tx})}\}$, $\overline{H} = \{H_{\max}^{(\text{rx})}, H_{\max}^{(\text{tx})}\}$, and $\underline{H} =$

$\{H_{\min}^{(\text{rx})}, H_{\min}^{(\text{tx})}\}$. These parameters define the boundaries of the integration region for both the transmitting and receiving CAPAs. Then, using the Gauss-Legendre quadrature method, the integral term in (C-1) can be approximated by

$$I \approx \sum_{i=1}^{N_x} \sum_{j=1}^{N_y} w_i w_j f(x_i, y_j) c_x c_y, \quad (\text{C-2})$$

where x_i and y_j are the roots of Legendre polynomials $P_{N_x}(x)$ and $P_{N_y}(y)$. Here, the weights can be specified by

$$w_i = \frac{2}{(1 - x_i^2) [P'_{N_x}(x_i)]^2},$$

$$w_j = \frac{2}{(1 - y_j^2) [P'_{N_y}(y_j)]^2}.$$

where $P'_N(\cdot)$ represents the the first-order derivative of N -th Legendre polynomials evaluated at $(\cdot) = \{x_i, y_i\}$. By capitalizing on the Gauss-Legendre quadrature method, we can convert all the integrals into multiple summations.

REFERENCES

- [1] W. Jiang, Q. Zhou, J. He, M. A. Habibi, S. Melnyk, M. El-Absi, B. Han, M. D. Renzo, H. D. Schotten, F.-L. Luo, T. S. El-Bawab, M. Juntti, M. Debbah, and V. C. M. Leung, "Terahertz communications and sensing for 6G and beyond: A comprehensive review," *IEEE Commun. Surv. Tut.*, vol. 26, no. 4, pp. 2326–2381, Apr. 2024.
- [2] A. A. D'Amico, A. d. J. Torres, L. Sanguinetti, and M. Win, "Cramér-Rao bounds for holographic positioning," *IEEE Trans. Signal Process.*, vol. 70, pp. 5518–5532, Nov. 2022.
- [3] Z. Wang, X. Mu, and Y. Liu, "Rethinking integrated sensing and communication: When near field meets wideband," *IEEE Commun. Mag.*, vol. 62, no. 9, pp. 44–50, Sept. 2024.
- [4] E. Björnson, F. Kara, N. Kolomvakis, A. Kosasih, P. Ramezani, and M. Salman, "Enabling 6G performance in the upper mid-band through gigantic MIMO," *arXiv preprint arXiv:2407.05630*, 2024.
- [5] Y. Liu, C. Ouyang, Z. Wang, J. Xu, X. Mu, and Z. Ding, "CAPA: Continuous-aperture arrays for revolutionizing 6G wireless communications," *arXiv preprint arXiv:2412.00894*, 2024.
- [6] Y. Liu, Z. Wang, J. Xu, C. Ouyang, X. Mu, and R. Schober, "Near-field communications: A tutorial review," *IEEE Open J. Commun. Soc.*, vol. 4, pp. 1999–2049, Aug. 2023.
- [7] Y.-D. Huang and M. Barkat, "Near-field multiple source localization by passive sensor array," *IEEE Trans. Antennas Propag.*, vol. 39, no. 7, pp. 968–975, Aug. 1991.
- [8] X. Zhang, W. Chen, W. Zheng, Z. Xia, and Y. Wang, "Localization of near-field sources: A reduced-dimension MUSIC algorithm," *IEEE Commun. Lett.*, vol. 22, no. 7, pp. 1422–1425, May 2018.
- [9] Z. Wang, X. Mu, and Y. Liu, "Near-field integrated sensing and communications," *IEEE Commun. Lett.*, vol. 27, no. 8, pp. 2048–2052, May 2023.
- [10] M. N. E. Korso, R. Boyer, A. Renaux, and S. Marcos, "Conditional and unconditional Cramér-Rao bounds for near-field source localization," *IEEE Trans. Signal Process.*, vol. 58, no. 5, pp. 2901–2907, May 2010.
- [11] L. Khamidullina, I. Podkurkov, and M. Haardt, "Conditional and unconditional Cramér-rao bounds for near-field localization in bistatic mimo radar systems," *IEEE Trans. Signal Process.*, vol. 69, pp. 3220–3234, May 2021.
- [12] Z. Wang, X. Mu, and Y. Liu, "Near-field velocity sensing and predictive beamforming," *IEEE Trans. Veh. Technol.*, pp. 1–6, early access.
- [13] C. Giovannetti, N. Decarli, and D. Dardari, "Performance bounds for velocity estimation with extremely large aperture arrays," *IEEE Wireless Commun. Lett.*, pp. 1–1, early access.
- [14] A. Chen, L. Chen, Y. Chen, C. You, G. Wei, and F. R. Yu, "Cramér-Rao bounds of near-field positioning based on electromagnetic propagation model," *IEEE Trans. Veh. Technol.*, vol. 72, no. 11, pp. 13 808–13 825, Jun. 2023.
- [15] A. Chen, L. Chen, Y. Chen, N. Zhao, and C. You, "Near-field positioning and attitude sensing based on electromagnetic propagation modeling," *IEEE J. Sel. Areas Commun.*, vol. 42, no. 9, pp. 2179–2195, Jun. 2024.
- [16] F. Liu, Y. Cui, C. Masouros, J. Xu, T. X. Han, Y. C. Eldar, and S. Buzzi, "Integrated sensing and communications: Toward dual-functional wireless networks for 6G and beyond," *IEEE J. Sel. Areas Commun.*, vol. 40, no. 6, pp. 1728–1767, Mar. 2022.
- [17] Z. Zhang and L. Dai, "Pattern-division multiplexing for multi-user continuous-aperture MIMO," *IEEE J. Sel. Areas Commun.*, vol. 41, no. 8, pp. 2350–2366, Apr. 2023.
- [18] B. Zhao, C. Ouyang, X. Zhang, and Y. Liu, "Continuous aperture array (CAPA)-based wireless communications: Capacity characterization," *arXiv:2406.15056*, 2024.
- [19] M. Qian, L. You, X.-G. Xia, and X. Gao, "On the spectral efficiency of multi-user holographic MIMO uplink transmission," *IEEE Trans. Wireless Commun.*, pp. 1–1, early access, 2024, doi: 10.1109/TWC.2024.3429495.
- [20] A. Pizzo, L. Sanguinetti, and T. L. Marzetta, "Fourier plane-wave series expansion for holographic MIMO communications," *IEEE Trans. Wireless Commun.*, vol. 21, no. 9, pp. 6890–6905, Sept. 2022.
- [21] L. Sanguinetti, A. A. D'Amico, and M. Debbah, "Wavenumber-division multiplexing in line-of-sight holographic MIMO communications," *IEEE Trans. Wireless Commun.*, vol. 22, no. 4, pp. 2186–2201, Sept. 2023.
- [22] Z. Wang, C. Ouyang, and Y. Liu, "Beamforming optimization for continuous aperture array (CAPA)-based communications," *arXiv preprint arXiv:2410.13677*, 2024.
- [23] C. Ouyang, Z. Wang, B. Zhao, X. Zhang, and Y. Liu, "On the impact of reactive region on the near-field channel gain," *IEEE Commun. Lett.*, vol. 28, no. 10, pp. 2417–2421, Jul. 2024.
- [24] E. Björnson and L. Sanguinetti, "Power scaling laws and near-field behaviors of massive MIMO and intelligent reflecting surfaces," *IEEE Open J. Commun. Soc.*, vol. 1, pp. 1306–1324, Sept. 2020.
- [25] A. Poon, R. Brodersen, and D. Tse, "Degrees of freedom in multiple-antenna channels: a signal space approach," *IEEE Trans. Inf. Theory*, vol. 51, no. 2, pp. 523–536, Feb. 2005.
- [26] M. A. Jensen and J. W. Wallace, "Capacity of the continuous-space electromagnetic channel," *IEEE Trans. Antennas Propag.*, vol. 56, no. 2, pp. 524–531, Feb. 2008.
- [27] F. Liu, Y.-F. Liu, A. Li, C. Masouros, and Y. C. Eldar, "Cramér-rao bound optimization for joint radar-communication beamforming," *IEEE Trans. Signal Process.*, vol. 70, pp. 240–253, Dec. 2022.
- [28] X. Song, J. Xu, F. Liu, T. X. Han, and Y. C. Eldar, "Intelligent reflecting surface enabled sensing: Cramér-Rao bound optimization," *IEEE Trans. Signal Process.*, vol. 71, pp. 2011–2026, May 2023.
- [29] J. Li, L. Xu, P. Stoica, K. W. Forsythe, and D. W. Bliss, "Range compression and waveform optimization for MIMO radar: A Cramér-Rao bound based study," *IEEE Trans. Signal Process.*, vol. 56, no. 1, pp. 218–232, Dec. 2008.
- [30] X. Yu, J.-C. Shen, J. Zhang, and K. B. Letaief, "Alternating minimization algorithms for hybrid precoding in millimeter wave MIMO systems," *IEEE J. Sel. Topics Signal Process.*, vol. 10, no. 3, pp. 485–500, Feb. 2016.
- [31] K. Alhujaili, V. Monga, and M. Rangaswamy, "Transmit mimo radar beampattern design via optimization on the complex circle manifold," *IEEE Trans. Signal Process.*, vol. 67, no. 13, pp. 3561–3575, May 2019.
- [32] K. B. Petersen and M. S. Pedersen, "The matrix cookbook," Nov 2012. [Online]. Available: <https://www.math.uwaterloo.ca/~hwolkowi/matrixcookbook.pdf>
- [33] Z.-q. Luo, W.-k. Ma, A. M.-c. So, Y. Ye, and S. Zhang, "Semidefinite relaxation of quadratic optimization problems," *IEEE Signal Process. Mag.*, vol. 27, no. 3, pp. 20–34, Apr. 2010.
- [34] H. Hua, J. Xu, and R. Zhang, "Near-field integrated sensing and communication with extremely large-scale antenna array," *arXiv preprint arXiv:2407.17237*, 2024.
- [35] S. M. Kay, *Fundamentals of Statistical Signal Processing: Estimation Theory*. Englewood Cliff, NJ, USA: Prentice Hall, 1993.
- [36] J. Guo, Y. Liu, H. Shin, and A. Nallanathan, "Deep learning for beamforming in multi-user continuous aperture array (CAPA) systems," *arXiv preprint arXiv:2411.09104*, 2024.